

# Reconciling stellar dynamical and hydrostatic X-ray mass measurements of an elliptical galaxy with gas rotation, turbulence and magnetic fields

Philip J. Humphrey<sup>1</sup>, David A. Buote<sup>1</sup>, Fabrizio Brighenti<sup>2,3</sup>, Karl Gebhardt<sup>4</sup> and William G. Mathews<sup>3</sup>

<sup>1</sup> Department of Physics and Astronomy, University of California, Irvine, 4129 Frederick Reines Hall, Irvine, CA 92697-4575

<sup>2</sup> Dipartimento di Astronomia, Università di Bologna, Via Ranzani 1, Bologna 40127, Italy

<sup>3</sup> University of California Observatories, Lick Observatory, University of California at Santa Cruz, Santa Cruz, CA 95064

<sup>4</sup> Astronomy Department, University of Texas, Austin, TX 78712

24 June 2018

## ABSTRACT

Recent hydrostatic X-ray studies of the hot interstellar medium (ISM) in early-type galaxies underestimate the gravitating mass as compared to stellar dynamics, implying modest, but significant deviations from exact hydrostatic equilibrium. We present a method for combining X-ray measurements and stellar dynamical constraints in the context of Bayesian statistics that allows the radial distribution of the implied non-thermal pressure or bulk motions in the hot ISM to be constrained. We demonstrate the accuracy of the method with hydrodynamical simulations tailored to produce a realistic galaxy model. Applying the method to the nearby elliptical galaxy NGC 4649, we find a significant but subdominant nonthermal pressure fraction ( $0.27 \pm 0.06$ ) in the central ( $\lesssim 5$  kpc) part of the galaxy, similar to the level of deviations from hydrostatic equilibrium expected in galaxy clusters. Plausible sources of systematic error, if important, may reduce this fraction. Our results imply  $\sim 360 \text{ km s}^{-1}$  random turbulence or a magnetic field  $B = (39 \pm 6)(n_e/0.1 \text{ cm}^{-3})^{0.59 \pm 0.09} \mu\text{G}$ , whereas gas rotation alone is unlikely to explain the detailed nonthermal profile. Future observations with *Astro-H* will allow turbulence or gas rotation at this level to be detected.

**Key words:** galaxies: elliptical and lenticular, cD— galaxies: ISM— galaxies: magnetic fields— galaxies: kinematics and dynamics— turbulence— X-rays: galaxies

## 1 INTRODUCTION

The distribution of mass in early-type galaxies is a fundamental yardstick for understanding their formation and evolution. Our current  $\Lambda$ CDM cosmological paradigm predicts ubiquitous, massive dark matter halos, the distribution of matter within which correlates with the mass of the system (e.g. Navarro et al. 1997; Bullock et al. 2001; Macciò et al. 2008). Within the optical radius of the galaxy, the relative contributions to the gravitational potential of the dark and luminous matter may explain the tilt of the fundamental plane (e.g. Cappellari et al. 2006; Bolton et al. 2007; Humphrey & Buote 2010), and provide insights into the poorly understood processes by which they interact gravitationally, in particular the interplay between adiabatic contraction and dynamical friction (e.g. Blumenthal et al. 1986; Gnedin et al. 2004; El-Zant et al. 2004; Humphrey et al. 2006; Dutton et al. 2007; Gnedin et al. 2007; Abadi et al. 2010; Napolitano et al. 2010; Macciò et al. 2012). The stellar mass-to-light (M/L) ratio can provide important constraints

on the history of star formation and the shape, and universality, of the stellar initial mass function (IMF) (e.g. Gerhard et al. 2001; Gnedin et al. 2007; Humphrey et al. 2009; Treu et al. 2010; Cappellari et al. 2012). Furthermore, at the smallest scales, the tight relations between the central supermassive black hole (SMBH) mass and the global properties of the host galaxy imply strong evolutionary symbiosis (e.g. Kormendy & Richstone 1995; Gebhardt et al. 2000; Merritt & Ferrarese 2001; Gültekin et al. 2009; Ferrarese & Ford 2005, for a review).

A number of techniques are available to study the mass distributions in early-type galaxies, each having its own distinct advantages and disadvantages. For example, gravitational lensing studies directly probe the projected mass distribution, but alone they do not generally produce detailed mass profiles for individual giant elliptical galaxies, although they can provide important constraints on the profile averaged over multiple systems (e.g. Gavazzi et al. 2007), or when combined with stellar dynamics measurements (e.g.

Koopmans et al. 2009; Barnabè et al. 2011). By combining information from multiple dynamical tracers, sophisticated (axisymmetric) orbit-based (stellar) dynamical models are now able to probe from within the sphere of influence of the SMBH out to tens of kpc (e.g. Romanowsky et al. 2003; Gebhardt & Thomas 2009), but models self-consistently incorporating dark matter halos can be computationally costly to evaluate (e.g. Shen & Gebhardt 2010), and care must be taken to minimize systematic uncertainties associated with their implementation (e.g. Valluri et al. 2004; Shen & Gebhardt 2010; Das et al. 2011; Long & Mao 2012) and the (generally) unknown inclination of the system (Gavazzi 2005; Thomas et al. 2007).

Hydrostatic X-ray techniques, on the other hand, are appealing in part due to their computational simplicity, given the isotropy of the gas pressure tensor and the fact that the spherical approximation (which is generally assumed, although not exclusively; e.g. Buote & Canizares 1994, 1996, 1998; Buote et al. 2002; Statler & McNamara 2002) typically introduces only a small bias (Buote & Humphrey 2012c, and references therein), particularly if the spherically averaged mass profile is close to a singular isothermal sphere (Buote & Humphrey 2012b; Churazov et al. 2008), which is generally true in early-type galaxies (e.g. Koopmans et al. 2009; Humphrey & Buote 2010; Churazov et al. 2010a). These methods are especially powerful since current instrumentation allows measurements from close to the sphere of influence of the most massive nearby black holes out to  $\gtrsim R_{2500}$  for some nearby galaxies (Humphrey et al. 2008, 2009, 2011, 2012b; Wong et al. 2011; Buote & Humphrey 2012a, for a review), and the same approach can be applied self-consistently from  $\sim$ Milky Way-mass galaxies to massive clusters.

The accuracy of hydrostatic methods is, naturally, contingent on the extent to which equilibrium gas motions reflect the thermal gas pressure rather than turbulent or streaming motions. To ensure systems are not grossly far from equilibrium and do not exhibit dynamically dominant, supersonic gas motions, excluding objects with highly asymmetric X-ray isophotes is an important first step (Buote & Humphrey 2012a). Nevertheless, subsonic gas motions (either bulk or turbulent), or nonthermal support from magnetic fields or cosmic rays could still be important (e.g. Churazov et al. 2008). Cosmic ray pressure is likely to be most important in the vicinity of cavities inflated by an AGN jet (e.g. Mathews & Brighenti 2008). Magnetic fields weaker than a few  $\mu\text{G}$  in the centre of the galaxy should not be dynamically important (Buote & Humphrey 2012a), but there is considerable uncertainty on the actual magnetic field strength, with current observational constraints from galaxies with embedded radio jets ranging from  $\sim 1\mu\text{G}$  to a few tens of  $\mu\text{G}$  (Vallée 2011).

Interesting constraints on gas dynamics are few (Buote & Humphrey 2012a). The upper limits on X-ray spectral line broadening ( $\sim 400\text{--}500\text{km s}^{-1}$ , from *XMM* RGS observations: Sanders et al. 2011), and velocity gradients ( $\sim 1000\text{--}2000\text{km s}^{-1}$  from the spatial variation of the X-ray line centroids in clusters: Ota et al. 2007; Sato et al. 2008; Sugawara et al. 2009; Tamura et al. 2011) exceed the typical circular velocity for a giant elliptical galaxy. Indirect gas dynamical constraints in the very centres of early-type galaxies can be obtained from resonance scattering (or its absence) in strong

emission lines (Churazov et al. 2010b, for a review). Current measurements suggest microturbulent velocities ranging from  $\sim 300\text{--}700\text{km s}^{-1}$  and  $100\text{--}500\text{km s}^{-1}$  respectively in two giant elliptical galaxies (albeit sensitive to the fitted plasma code; de Plaa et al. 2012), to  $\lesssim 100\text{km s}^{-1}$  in the centre of the elliptical galaxy NGC 4636 (Xu et al. 2002; Werner et al. 2009, who also found evidence of little turbulence in two other galaxies). The interpretation of these results, however, may be complicated by the scale and anisotropy of the turbulence (Zhuravleva et al. 2011). Dynamically important gas rotation, such as expected in subsonically inflowing gas due to angular momentum conservation, should result in a flattening of the X-ray isophotes parallel to the rotation axis. This allowed Brighenti et al. (2009, hereafter B09) to infer  $\sim 200\text{--}300\text{km s}^{-1}$  gas motions in the central  $\sim$ kpc of the elliptical galaxy NGC 4649, and led them to suggest that inflowing, rotating gas may be common in the very central parts of nearby elliptical galaxies.

A direct assessment of the accuracy of hydrostatic methods in an elliptical galaxy can be made by comparing the mass inferred from the X-rays to that obtained by independent techniques. Orbit-based stellar dynamical models are the alternative method of choice for nearby systems, as they provide high-quality mass profiles that overlap well in radial scale with X-ray work. To date such comparisons have been made reliably in only a handful of cases. Gebhardt & Thomas (2009) found inconsistency between their axisymmetric dynamical models for M 87 and the gravitational potential inferred from X-rays by Churazov et al. (2008). Das et al. (2010) and Murphy et al. (2011) quantified this discrepancy further, finding that the X-rays underestimate the optically inferred mass by  $\sim 50\%$  within the central  $\sim 4$  kpc, while the data generally agreed at larger scales. M 87 exhibits, however, substantial disturbances to its X-ray morphology (e.g. Böhringer et al. 1994; Forman et al. 2007; Million et al. 2010), which may introduce systematic uncertainties into a single-phase spherical hydrostatic mass analysis. Shen & Gebhardt (2010) found that the X-ray inferred mass that was measured by Humphrey et al. (2008) for the elliptical galaxy NGC 4649 was  $\sim 40\%$  lower than their dynamical models implied inside  $\sim 8$  kpc, despite its very smooth, relaxed X-ray isophotes. A similar result was obtained by Das et al. (2010), who also compared their X-ray determined mass profile for NGC 4472 to (unpublished) orbit-based models, finding it to be  $\sim 30\%$  lower inside  $\sim 10$  kpc but  $\sim 20\%$  higher further out. This dichotomy may, in part, reflect X-ray disturbances in the system at the largest scales (Irwin & Sarazin 1996; Biller et al. 2004). Rusli et al. (2011) measured the mass distribution in the central regions of the lenticular galaxy NGC 1332 with axisymmetric orbit-based models (excluding a dark matter halo), and finding the X-ray inferred profile obtained by Humphrey et al. (2009) to be  $\sim 50\%$  lower.

A number of other studies are less definitive due to limitations in the optical or X-ray analysis. For example, Norris et al. (2012) derived the mass of NGC 3923 from axisymmetric orbit-based models, including a dark matter halo, finding an offset from the X-ray mass profile of Fukazawa et al. (2006). Although corrections were applied to account for unresolved sources when computing the temperature, Fukazawa et al. did not account for this contamination when deriving the density profile. An independent *Rosat* study by

Buote & Canizares (1998), considering non-spherical mass models for this galaxy, was actually in better agreement with the dynamical mass. Several authors have compared X-ray inferred masses with simpler dynamical models that may be less reliable (e.g. Mathews & Brighenti 2003b; Ciotti & Pellegrini 2004; Churazov et al. 2008, 2010a; Romanowsky et al. 2009; Johnson et al. 2009; Das et al. 2010), or have used X-ray mass profiles that are likely unreliable due to large morphological disturbances (e.g. NGC 4636: Johnson et al. 2009; NGC 5846: Churazov et al. 2010a; Das et al. 2010), unresolved point source contamination (Pellegrini & Ciotti 2006), or systematic uncertainties associated with the model parameterizations (Romanowsky et al. 2009).

Based on these studies, a consistent picture is beginning to emerge of X-ray hydrostatic methods underestimating the mass inferred from stellar dynamical techniques by *on average*  $\sim 30\text{--}50\%$  in the central part of the galaxy. Understanding this discrepancy is essential not only in order to correct hydrostatic mass for this effect, but also to gain insight into the behaviour and fate of the gas at the centre of a galaxy-scale cooling flow (Mathews & Brighenti 2003a). Obtaining detailed radial profiles of the measured nonthermal pressure or bulk gas motions is a critical next step. While, in essence, this can be achieved by differencing the mass profiles inferred by both techniques, most recent studies have only compared them approximately (e.g. Shen & Gebhardt 2010; Das et al. 2010, 2011; Rusli et al. 2011; Murphy et al. 2011; Norris et al. 2012)<sup>1</sup>

Given that the level of discrepancy is  $\lesssim 50\%$ , it is crucial to control tightly the systematic uncertainties in both the X-ray and stellar dynamical measurements. From an X-ray perspective, there are a number of ways to infer the gravitating mass from X-ray data, as reviewed in Buote & Humphrey (2012a). For a reliable measurement, however, any fitted models must have sufficient flexibility to capture the full range of physical gas temperature and density profiles. The traditional “smoothed inversion” technique, as widely employed in studying galaxy clusters, involves fitting parameterized models directly to the density and temperature distributions but, due to their diverse shapes in elliptical galaxies, there are in general no well-defined “universal” parameterizations that can be employed, introducing potentially large systematic uncertainties in this regime (e.g. Humphrey et al. 2009; Buote & Humphrey 2012a). Das et al. (2010) proposed a minimally parametric “smoothed inversion” technique that does not *a priori* restrict the form of the density and temperature profiles, but it does employ a certain level of smoothing. We discuss the performance of this method in the Appendix. In practice, we have found an entropy-based “forward fitting” approach to be an attractive means for computing the mass profile reliably, as it rigorously enforces both a physical mass distribution and Schwarzschild’s stability criterion for the ISM (Humphrey

<sup>1</sup> We note that if one compares the difference between two radii in the *potential* (rather than the enclosed mass) that is obtained with each method, as advocated by Churazov et al. (2008), the average nonthermal pressure in that range can also be derived. The interpretation is complicated, however, by the lack of statistical independence between the potential “data-points” generated in this way. Nevertheless, Churazov et al. used this approach to infer the *global average* level of support in two objects.

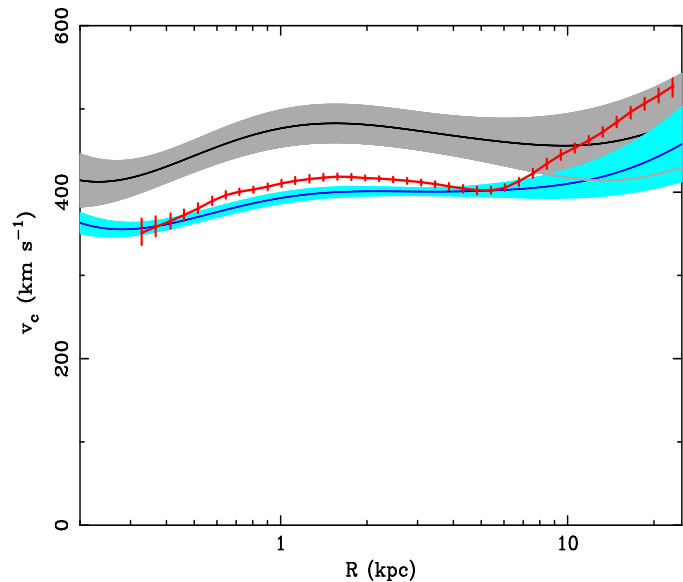


**Figure 1.** Comparison of the circular velocity profile of NGC 4649 derived from the stellar dynamical analysis of Shen & Gebhardt (2010, grey region), and our purely hydrostatic analysis of the hot ISM (blue shaded region). We also show (red) the best-fitting model and  $1\text{-}\sigma$  confidence region obtained by Das et al. (2010) from their hydrostatic X-ray analysis. The modest discrepancies between the X-ray measurements likely arise from different modelling assumptions in the Das et al. analysis (see the Appendix), while the higher optical measurement can be interpreted as arising from modest nonthermal pressure.

et al. 2008, 2009, 2011). The drawback of this technique for computing the nonthermal pressure profile is that it assumes the mass inferred by hydrostatic techniques can be well-parameterized by the same model that can fit the true mass distribution, which need not be true in the case of a nonthermal pressure gradient.

In this paper, we develop a simple extension of the entropy-based, forward fitting technique that incorporates non-hydrostatic effects. This method allows the radial distribution of the nonthermal pressure or gas motions to be constrained directly from a joint, Bayesian analysis of the X-ray and stellar dynamics data. We illustrate the performance of the method both with simulated galaxies, and with a real system (NGC 4649), and interpret the results in terms of physical models for the gas flow, turbulence and possible magnetic fields. In what follows, all error bars correspond to  $1\text{-}\sigma$  uncertainty.

## 2 NGC 4649

To test our method, and provide important constraints on a well-studied system, we focused our analysis on NGC 4649. This is a nearby (15.7 Mpc)<sup>2</sup>, giant elliptical galaxy with a luminous X-ray halo and a remarkably round, relaxed X-ray morphology, at least within  $\sim 20$  kpc (Trinchieri et al. 1997; Randall et al. 2004; Humphrey et al. 2008). Low significance surface brightness asymmetries were reported in a shallow

<sup>2</sup> We adopt a distance of 15.7 Mpc for consistency with the dynamical models of Shen & Gebhardt (2010)

*Chandra* observation by Randall et al. (2004), which they, in part, speculated may arise due to convective flows. This hypothesis is inconsistent, however, with the monotonically rising entropy profile (implying global stability against convection). In any case, the features were not confirmed in deeper *Chandra* observations (Humphrey et al. 2008). Shurkin et al. (2008) reported the detection of small cavities associated with the weak radio jet but these were also not confirmed in our deeper data. Instead the gas was found to be very symmetrical and relaxed-looking (Humphrey et al. 2008). The X-ray isophotes do exhibit central flattening, however, which suggests that gas rotation may be important in the central  $\sim 1$  kpc (B09).

Given its proximity and high surface brightness, we were able to measure the gas properties from close to the sphere of influence of the central black hole ( $\sim 1''$ ) out to  $\sim 25$  kpc, allowing, for the first time, the mass of *any* SMBH to be inferred directly from a hydrostatic X-ray model (Humphrey et al. 2008). State of the art, orbit-based, axisymmetric stellar dynamical models, which spanned a similar radial range, were constructed by Shen & Gebhardt (2010), assuming an edge-on geometry (but verifying that the results were not very sensitive to the adopted inclination). Although the inferred black hole mass was in statistical agreement with the X-ray measurement, they found a modest discrepancy with the hydrostatic mass profile within the central  $\sim 8$  kpc. A similar discrepancy was noted by Das et al. (2010) between the dynamical mass of Shen & Gebhardt and their own X-ray mass model.

In Fig 1 we show the circular velocity ( $v_c = \sqrt{GM/r}$ , where  $G$  is the Universal gravitational constant and  $M$  is the total mass enclosed within radius  $r$ ) profile for NGC 4649, based on the X-ray data (Humphrey et al. 2008) and the dynamical analysis of Shen & Gebhardt (2010)<sup>3</sup>, illustrating the offset between the inferred mass distributions. We also overlay the  $v_c$  profile of Das et al. (2010), which overall agrees well with our measurement over the range  $\sim 3$ – $9$  kpc, but is marginally higher outside this range. We ascribe these differences to particular choices made in their analysis (see the Appendix for a more detailed discussion). The generally good agreement between the two X-ray measurements indicates that the level of discrepancy with the optical results is not sensitive to the details of the X-ray modelling although, as discussed in the Appendix, the error bars may be.

In the present study, we interpret the offset between the X-ray and dynamical measurements as wholly arising due to deviations from hydrostatic equilibrium. Naturally, this is contingent upon the optical result being an unbiased measurement of the true gravitational potential. For the state of the art models used by Shen & Gebhardt (2010), which have previously shown to perform well in recovering the mass of simulated galaxies, we do not expect there to be significant inherent systematic uncertainties, other than a dependence on the viewing angle (Thomas et al. 2007). We therefore assume that the gravitational potential inferred by Shen & Gebhardt (2010) is accurate. We note that, recently, Das et al. (2011) constructed “made to measure” particle-based

models for the system (using the same kinematics data in the central region), finding larger statistical errors than Shen & Gebhardt, and thus formal consistency with the X-ray profile. However, investigating the origin of such systematic differences is beyond the scope of the present paper.

In order to constrain the nonthermal pressure profile, we carried out a joint analysis of the optical and X-ray data, as described in § 3.2. For the X-ray data, we used the published gas density and temperature profiles from Humphrey et al. (2008). For the optical constraints, we used the posterior probability distribution obtained by Shen & Gebhardt (2010) and linearly interpolated over their grid of  $\chi^2$  values (and assumed flat priors for each parameter).

### 3 MEASURING NONTHERMAL PRESSURE

#### 3.1 Preliminaries

If the ISM is in an equilibrium state and the magnetic fields are tangled, the total gravitating mass,  $M$ , enclosed within a surface  $\mathbf{S}$  is given by (Fang et al. 2009):

$$M = \frac{1}{4\pi G} \int_{\mathbf{S}} \left[ -\frac{1}{\rho_g} \nabla P - (\mathbf{v} \cdot \nabla) \mathbf{v} \right] \cdot d\mathbf{S} \quad (1)$$

where  $G$  is the universal gravitational constant,  $\rho_g$  is the gas density,  $P$  is the total pressure (including thermal gas pressure, and pressure from tangled magnetic fields, cosmic rays and turbulence),  $\mathbf{v}$  is the (time averaged) gas velocity field and  $d\mathbf{S}$  a surface element. Assuming  $\mathbf{S}$  is a spherical surface of radius  $r$ , this becomes:

$$\frac{v_c^2}{r} = \frac{1}{4\pi} \int_{4\pi} -\frac{1}{\rho_g} \frac{dP}{dr} d\Omega - \frac{1}{4\pi} \int_{4\pi} \hat{\mathbf{r}} \cdot (\mathbf{v} \cdot \nabla) \mathbf{v} d\Omega \quad (2)$$

where  $v_c$  is the circular velocity,  $\Omega$  is the solid angle, and  $\hat{\mathbf{r}}$  is the unit vector in the radial direction. For convenience, we define  $\langle \rho_g \rangle$  such that

$$\frac{1}{\langle \rho_g \rangle} \frac{d \langle P \rangle}{dr} \equiv \frac{1}{4\pi} \int_{4\pi} \frac{1}{\rho_g} \frac{dP}{dr} d\Omega \quad (3)$$

where  $\langle P \rangle$  is the spherically averaged pressure. We also define an “effective” gas velocity,  $v_{eff}$ , such that

$$\frac{v_{eff}^2}{r} \equiv -\frac{1}{4\pi} \int_{4\pi} \hat{\mathbf{r}} \cdot (\mathbf{v} \cdot \nabla) \mathbf{v} d\Omega \quad (4)$$

To make further progress, we assume that the density and pressure are approximately stratified on concentric spheres, which is generally a good approximation (Buote & Humphrey 2012b,c, and references therein). In that case, we can drop the  $\langle \rangle$  averaging notation in Eqn 3. If the only dynamically important gas motions are rotation about a common axis (i.e.  $\mathbf{v} = v_\phi \mathbf{e}_\phi$  where  $\mathbf{e}_\phi$  is the unit vector in the  $\phi$  direction in spherical coordinates),  $v_{eff}^2 = \int_{4\pi} v_\phi^2 d\Omega / 4\pi$ ; hence  $v_{eff}$  would be a spherically averaged gas rotation velocity.

We define  $P \equiv P_g / (1 - f_{nth})$ , where  $P_g$  is the thermal gas pressure ( $P_g = \rho_g kT / (\mu m_H)$ ;  $k$  is Boltzmann’s constant,  $T$  is the gas temperature,  $\mu \simeq 0.62$  is the mean molecular weight, and  $m_H$  is the weight of hydrogen), and  $f_{nth}$  is the nonthermal pressure fraction. We also define  $S = \rho_g^{-2/3} kT / (\mu m_H)$ , which is proportional to the traditional definition of the entropy proxy,  $K = n_e^{-2/3} kT$ , where

<sup>3</sup> This Bayesian realization of the  $v_c$  profile was derived by linearly interpolating over the  $\chi^2$ -topology obtained by Shen & Gebhardt (2010) from their stellar dynamical analysis.

$n_e$  is the electron number density. Combining Eqns 2–4 and rearranging, we obtain

$$r^2 \left( \frac{S}{P_g} \right)^{\frac{3}{5}} \frac{d}{dr} \left( \frac{P_g}{1 - f_{nth}} \right) = -r [v_c^2 - v_{eff}^2] \quad (5)$$

Writing  $v_c^2 = v_{c,g}^2 + v_{c,ng}^2$ , where  $v_{c,g}$  is the circular velocity due to the gas mass, and  $v_{c,ng}$  is due to the non-gas mass, differentiating and folding in the gas mass continuity equation,

$$\frac{d}{dr} (r v_{c,g}^2) = 4\pi G r^2 \left( \frac{P_g}{S} \right)^{\frac{3}{5}} \quad (6)$$

we obtain:

$$\frac{d}{dr} \left[ r^2 \left( \frac{S}{P_g} \right)^{\frac{3}{5}} \frac{d}{dr} \left( \frac{P_g}{1 - f_{nth}} \right) \right] = -\frac{d}{dr} r [v_{c,ng}^2 - v_{eff}^2] - 4\pi G r^2 \left( \frac{P_g}{S} \right)^{\frac{3}{5}} \quad (7)$$

### 3.2 Method

Adopting parameterized models for  $S$ ,  $v_{c,ng}$ ,  $f_{nth}$  and  $v_{eff}$ , Eqn 7 can be integrated numerically, to solve for  $P$  using a fourth-order Runge-Kutta method. We start the integration at some arbitrary, small radius  $r_0$ . Two boundary conditions are needed; we set the thermal gas pressure at  $r_0$  to a value to be determined by our fit, and assume that the gas mass is zero within  $r_0$ . Since the model profiles of  $P_g$  and  $S$  uniquely determine the gas density and temperature, the observed temperature and density profiles can be fitted by adjusting the various model parameters. As the temperature and density are generally inferred by spherical deprojection of spectra accumulated in a series of concentric bins, to ensure a reliable comparison we integrated appropriately weighted functions of pressure and temperature to compute the predicted contribution to the emission measure (and hence mean density) from gas in the corresponding shell, as well as an emission-weighted temperature. We compared these averaged quantities to our measured temperature and density data points, as discussed in Humphrey et al. (2008) and Humphrey et al. (2009). See Appendix B of (Gastaldello et al. 2007b) for a detailed discussion of incorporating the plasma emissivity into the gas modelling.

To parameterize  $v_{c,ng}$ , we model the gravitating mass as arising from a central black hole, a stellar mass component (assuming mass follows light), plus a dark matter halo, which can either be a Navarro et al. (1997, hereafter NFW) profile, or a “cored logarithmic” potential (Binney & Tremaine 2008). The black hole mass, stellar M/L ratio, and normalization and characteristic scale of the dark matter component are adjustable fit parameters. To parameterize  $S$ , we adopt a multiply broken powerlaw, plus a constant term. This model has sufficient flexibility to capture the overall shapes of the entropy profiles in galaxy groups and clusters (e.g. Gastaldello et al. 2007a; Sun et al. 2009; Cavagnolo et al. 2009; Humphrey et al. 2012a). Since *a priori* there is no obvious parameterized form for  $f_{nth}$  or  $v_{eff}$ , we parameterize them with a cubic spline function. While the number of spline knots is arbitrary, we found the model to be generally well-behaved if there are roughly half as many knots as there are density (or temperature) bins, and they are placed

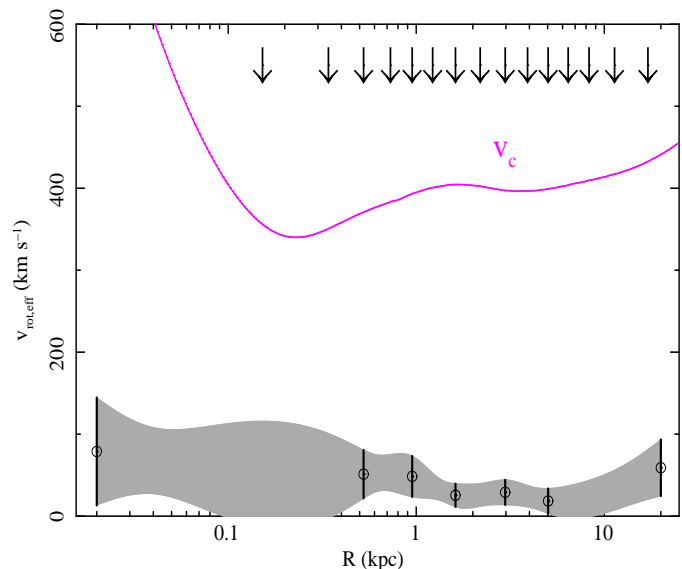


**Figure 2.** Recovered  $v_{eff}$  for the hydrostatic simulation. The data-points correspond to the spline knots fitted to the simulated data, and the grey region indicates the  $1-\sigma$  confidence region of the model interpolated between them. The magenta line is the circular velocity ( $v_c$ ; set to match the X-ray mass inferred by Humphrey et al. 2008), and the arrows indicate the approximate centre of each annulus used in the spectral analysis. The true  $v_{eff}$  distribution ( $v_{eff} = 0$ ) is consistent with the best fitting model, although there is a slight ( $\sim 30 \text{ km s}^{-1}$ ) bias, which is not dynamically important.

approximately logarithmically in radius. Since  $f_{nth}$  only appears inside the derivative in Eqn 7, a boundary condition on it is required. We therefore set  $f_{nth} = 0$  at large radii.

In the hydrostatic approximation,  $f \equiv 0$  and  $v_{eff} \equiv 0$  and so the two unknowns ( $S$  and  $v_c$ ) can be constrained completely by the two observables ( $\rho_g$  and  $kT$ ). By exploring parameter space with a Bayesian code (specifically, we use version 2.7 of the MultiNest code<sup>4</sup> (Feroz et al. 2009)), we can also fold in stellar dynamical constraints on  $v_c$  by using the posterior probability distribution from the dynamical analysis as priors on some of the parameters. In this case, we can relax the hydrostatic approximation and additionally measure the profile of *either*  $f_{nth}$  or  $v_{eff}$ . These two quantities are highly degenerate and so, without additional constraints, they cannot be disentangled uniquely. We therefore adopt the pragmatic approach of fitting each profile in turn, while setting the other term to zero.

### 3.3 Tests

To test the ability of our method to recover the nonthermal pressure profile in early-type galaxies, we used it to investigate two simulated datasets, each having different amounts of nonthermal support. Since our method involves directly fitting the X-ray data, and since we assume that the stellar dynamical constraints provide an unbiased estimate of the true gravitational potential, we considered the limit of perfect optical constraints, but a typical X-ray exposure

<sup>4</sup> <http://www.mrao.cam.ac.uk/software/multinest/>

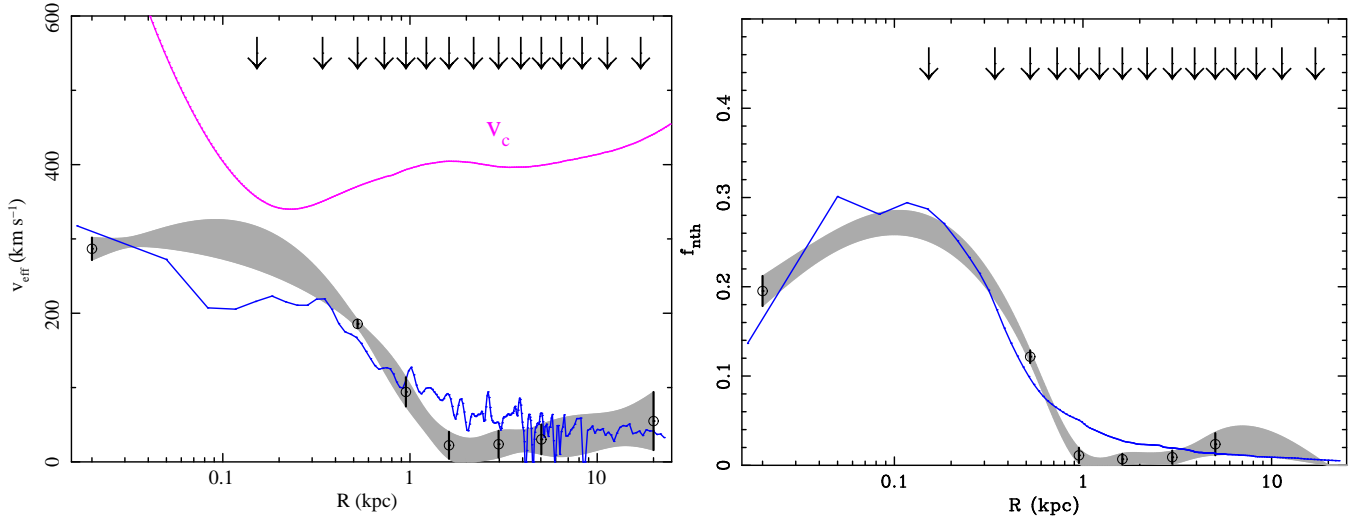


**Figure 3.** *Left:* Marginalized  $v_{eff}$  from fitting the B09 simulation. The data-points indicate the spline knots fitted to the simulation, and the grey region is the  $1-\sigma$  confidence region of the model interpolated between them. The blue line indicate the true profile of  $v_{eff}$ . The magenta line is the circular velocity (matching the mass inferred by Humphrey et al. 2008), and the arrows indicate the approximate centre of each annulus used in the spectral analysis. Overall, we find good agreement between the true distribution and the model. *Right:* The same nonthermal support profile parameterized as a nonthermal pressure fraction ( $f_{nth}$ ; grey shaded region and data-points), shown with the true profile (blue) and (arrows) the approximate centres of each radial bin. The overall fit is also fairly good. We note that the modest discrepancy between the true and inferred  $v_{eff}$  profiles around  $\sim 0.1\text{--}0.2$  kpc occurs between two spline knots and is mostly confined to the central radial bin, so we caution against over-interpretation.

(100 ks). The first of these datasets was derived assuming spherical symmetry and perfect hydrostatic equilibrium (i.e.  $v_{eff} \equiv f_{nth} \equiv 0$ ; hereafter the “hydrostatic simulation”). The second simulated dataset was based on the axisymmetric, hydrodynamical simulation performed by B09, in which there is turbulence and bulk gas motion. In both cases, the simulations were tailored to match approximately the properties of NGC 4649, as observed with *Chandra*.

For each simulated dataset, we started with the temperature, density and abundance of the gas as a function of position in an axisymmetric (R,z) grid, and created an artificial *Chandra* events file using a Monte Carlo method to generate photons. We assumed the source is at 15.7 Mpc, and the observation was 100 ks in duration. At each grid position, a random number of photons were generated, assuming an APEC plasma with the appropriate temperature and gas abundance, and using representative *Chandra* responses for close to the aimpoint. Each photon was randomly assigned a PHA (energy) bin and a spatial position within the bin, before being projected onto the sky. We processed the simulated events file similarly to the real *Chandra* data of NGC 4649 (Humphrey et al. 2008), which involves spherical deprojection with the *project* model in *Xspec vers 11*, and fitting an APEC plasma model with variable abundances, and produces the temperature, density and abundance profiles. Where appropriate, we tied the abundance between adjacent annuli, to improve constraints. To simplify the analysis, we filtered out photons originating from outside the outermost shell used in our deprojection.

We fitted the resulting temperature and density profiles simultaneously with our modified hydrostatic model, assuming flat priors on all fit parameters. In these tests, we aimed to determine how accurately the nonthermal pressure profile can be recovered in the limit of perfect dynamical data, so we

fixed the mass model parameters to match the true distribution used in the simulations. For the hydrostatic simulation, we show the recovered distribution of  $v_{eff}$  in Fig 2, demonstrating that the true distribution ( $v_{eff} = 0$ ) was reasonably well recovered. There was a slight ( $\sim 30 \text{ km s}^{-1}$ ) bias in the best-fitting velocity, which may reflect slight uncertainties in the deprojection procedure, but such a small velocity would be dynamically unimportant and so has minimal effect on our conclusions.

In Fig 3 (left panel) we show the fitted  $v_{eff}$  profile for the B09 simulation, along with its true distribution. Since the velocity field predicted by the simulation was known, we were able to compute the true  $v_{eff}$  profile by explicitly evaluating Eqn 4 (for more details of how this was done, see Fang et al. 2009). The fitted model was, by definition, a smooth function that cannot exactly capture all of the features in the true profile, but the overall shape was well recovered, especially in the vicinity of each spline knot. The largest deviations actually occurred within the central radial bin, at scales that are, effectively, unresolved. In the inner regions of the simulation ( $\lesssim 1$  kpc) the X-ray isophotes were quite flattened and there was a strong azimuthal temperature gradient (B09), so the spherical, single-phase approximation that is implicit in the deprojection method we adopted is a simplification. Despite this, the impact of these effects was modest and the recovered  $v_{eff}$  profile was sufficiently accurate for our purposes.

In Fig 3 (right panel), we show the fitted  $f_{nth}$  profile for the B09 simulation, and its true distribution. The nonthermal support in the simulation actually arises (mostly) from bulk gas motions rather than an additional pressure component. Still,  $f_{nth}$  and  $v_{eff}$  are highly degenerate, so we can still parameterize the nonthermal support as an “effective”  $f_{nth}$ . Writing out Eqn 5 for the two cases ( $v_{eff} \equiv 0$



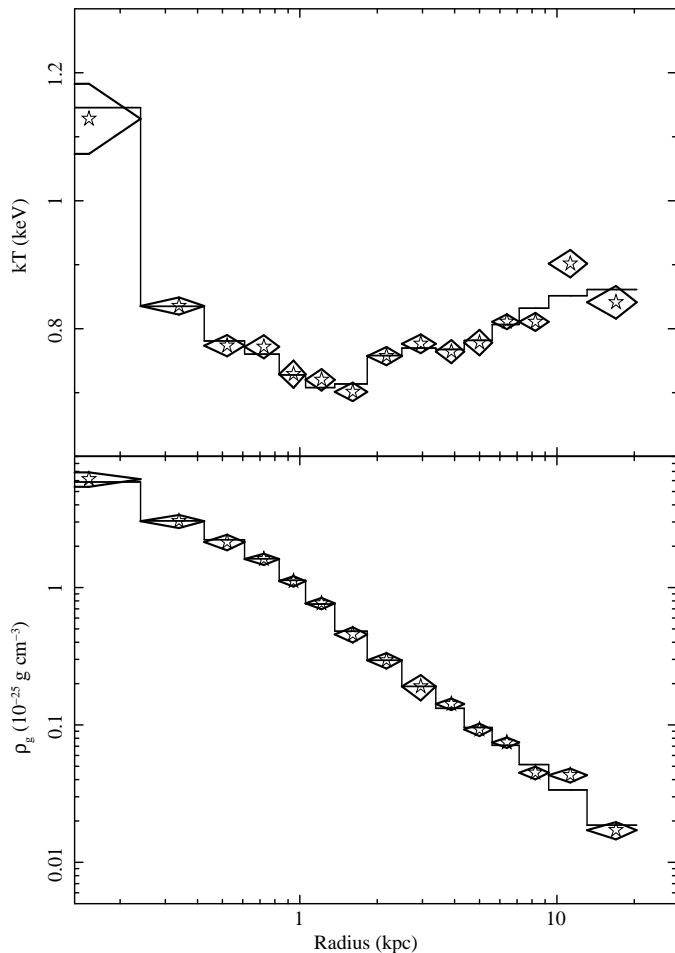


**Figure 4.** Profiles of  $kT$  (upper panel) and gas density (lower panel), along with the best-fitting model. Note the good agreement in all radial bins.

and  $f_{nth} \equiv 0$ ), and eliminating  $dP_g/dr$  between them, we find that  $f_{nth}$  and  $v_{eff}$  are related by:

$$v_{eff}^2 = f_{nth} v_c^2 + \frac{kT}{\mu m_H} \frac{d \log(1 - f_{nth})}{d \log r} \quad (8)$$

We integrated this equation numerically to obtain the “true”  $f_{nth}$ , which we found to be in good agreement with the fitted profile (Fig 3).

## 4 APPLICATION TO NGC 4649

### 4.1 Results

To study NGC 4649, we adopted the same parameterized gravitating mass model as Shen & Gebhardt (2010) (black hole, stellar component and a cored logarithmic dark matter mass model), and folded in the results of the stellar dynamical analysis as priors on the black hole mass, stellar M/L ratio and parameters of the dark matter model. For the stellar component, Shen & Gebhardt deprojected the V-band stellar light distribution from Kormendy et al. (2009), assuming an edge-on, oblate spheroidal geometry and a constant axis ratio of 0.9. Unlike the axisymmetric assumption of the dynamical analysis, the X-ray technique assumes spherical

geometry, and so it is important to average this profile spherically (Buote & Humphrey 2012b,c), which we did numerically.

We separately parameterized  $v_{eff}$  and  $f_{nth}$  as a 7-knot spline (each knot being placed approximately logarithmically in radius), and assuming flat priors on the model values at each knot point, within reasonable limits. The best-fitting model actually captured the shapes of the density and temperature profiles acceptably, although the  $f_{nth}$  parameterization is preferred ( $\chi^2=18.7/13$  and  $22.1/13$  for the  $f_{nth}$  and  $v_{eff}$  parameterizations, respectively; see Fig 4). The resulting  $v_{eff}$  and  $f_{nth}$  profiles are shown in Fig 5.

The shape of the  $v_{eff}$  profile is relatively flat, and could be consistent with a constant gas rotation velocity ( $v_{eff}=232 \pm 37 \text{ km s}^{-1}$ ), or with a mildly falling profile that becomes consistent with zero outside  $\sim 5$  kpc. Expressed in terms of  $f_{nth}$ , the profile is also consistent both with a constant nonthermal pressure fraction ( $f_{nth}=0.27 \pm 0.06$ ) or with a gradually declining distribution that becomes consistent with zero outside  $\sim 2$  kpc. Still, within  $\sim 2$  kpc, approximately  $\sim 30\%$  of the support must come from bulk gas motions or nonthermal pressure.

### 4.2 Systematic error budget

All methods for inferring the mass distributions in early-type galaxies entail arbitrary analysis choices, some of which may quantitatively affect the measured mass. In this section, we briefly explore how sensitive our conclusions are to the choices in the X-ray modelling. Further systematic uncertainties may be associated with choices in the stellar dynamical analysis (for example, the inclination angle assumed), but exploring them is beyond the scope of the present paper. The systematic error budget is summarized in Table 1, and we discuss below how each test was performed. For a more detailed discussion of the various systematic error assessments considered here, see Humphrey et al. (2012a).

We first examined the sensitivity of our spectral-fitting results to the treatment of the *Chandra* background (“ $\Delta$ Background”) by using the standard “background template” spectra, suitably renormalized to match the data at  $\gtrsim 10$  keV, instead of the more robust, modelled background adopted by default (Humphrey et al. 2008). We experimented with replacing the APEC thermal plasma model used in spectral fitting with the MEKAL model (“ $\Delta$ Spectral”) and varying the distance by  $\sim 33\%$  (corresponding to the statistical error on the distance to NGC 4649 given by Tonry et al. 2001, “ $\Delta$ Distance”). To investigate how changing the parameterized model used to fit the  $v_{eff}$  or  $f_{nth}$  profiles can affect the results, we experimented with reducing the number of spline knots to 3 (at 0.5 kpc, 0.16 kpc and 20 kpc), and also with using a constant  $v_{eff}$  or  $f_{nth}$  (“ $\Delta$ Knots”). These simpler parameterizations did not lead to significantly poorer fits. Next we examined how the choice of priors might be influencing our results by replacing each of the flat priors we adopted in our analysis by priors which were flat in logarithmic space (“ $\Delta$ Priors”). We also considered changing the entropy parameterization by adding an additional break at large radii (“ $\Delta$ Entropy”), experimented with folding in the full covariance between adjacent temperature and density data-points (“ $\Delta$ Covariance”) and turning off the emissivity computation when evaluating the

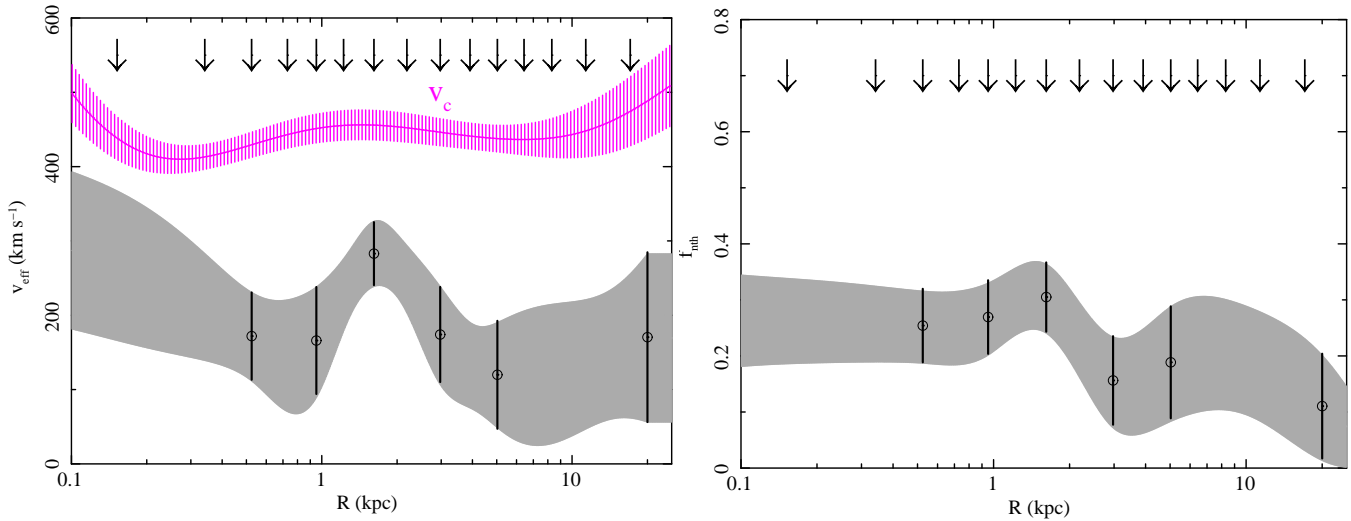


**Figure 5.** The same as Fig 3 but for the real NGC 4649 data. In this case the “true” profile is not shown as it is *a priori* unknown, and  $v_c$  is derived from the joint fit to the stellar dynamical and X-ray data.

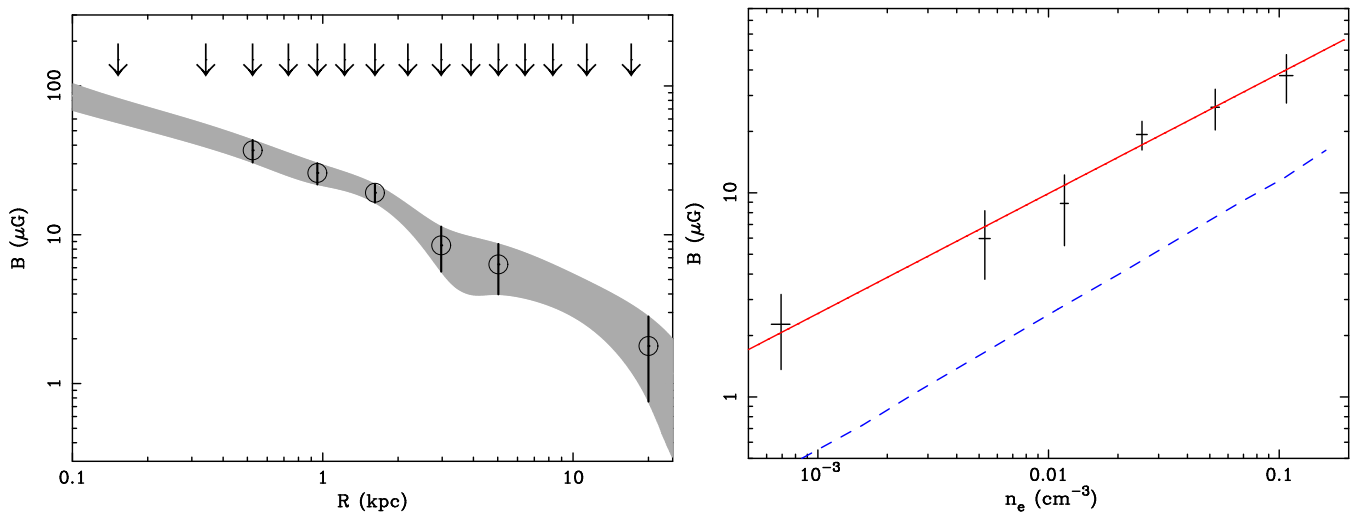


**Figure 6.** *Left panel:* The implied magnetic field profile in NGC 4649, assuming the nonthermal pressure comes from the B-field in equipartition with  $\sim 230 \text{ km s}^{-1}$  random turbulence. The data-points are the fitted spline points, while the grey region is the  $1\text{-}\sigma$  confidence range, interpolating between them. The arrows indicate the centres of each temperature and density data-bin. *Right panel:* The corresponding B-field *versus* electron density. The solid red line is the best-fitting powerlaw relation (see text). The dashed blue line is the prediction for the model of Mathews & Brighenti (1997, their Fig 2). The model slope agrees well with the observed data. The quoted uncertainties do not include systematic errors, including those from the stellar dynamical analysis. In particular, we note that, if the dynamical analysis of Das et al. (2011) is taken at face value, the implied level of nonthermal support may be lower than inferred here (see text).

weighted temperature and density models (“ $\Delta$ Weighting”; see Humphrey et al. 2012a for more details). We list the largest changes and statistical errors associated with each test in Table 1. In almost all cases, the change in the marginalized value was not much larger than the statistical error; in a few cases (especially at  $\sim 20 \text{ kpc}$ ) the statistical error-bars were enlarged by the test. Ultimately, none of the statistical uncertainties were large enough to lead to qualitatively different conclusions. Nonthermal support, approximately at the  $\sim 25\%$  level, is needed to reconcile the X-ray data with the published dynamical mass of NGC 4649.

## 5 DISCUSSION

### 5.1 A non-hydrostatic X-ray model

We have demonstrated that a simple modification to the entropy-based hydrostatic, forward fitting technique (Humphrey et al. 2008, 2009) allows nonthermal pressure profiles to be inferred from X-ray data, provided additional, unbiased, constraints on the mass profile are available (e.g. from stellar dynamical mass measurements). At scales resolved by the density and temperature profiles, the new technique was able to recover reasonably well the radial distributions of  $f_{nth}$  or  $v_{eff}$  in a simulated galaxy, which was



Test	$v_{eff}$ (0.5 kpc) (km s <sup>-1</sup> )	$v_{eff}$ (1.6 kpc) (km s <sup>-1</sup> )	$v_{eff}$ (20 kpc) (km s <sup>-1</sup> )	$f_{nth}$ (0.5 kpc)	$f_{nth}$ (1.6 kpc)	$f_{nth}$ (20 kpc)
Marginalized	191 ± 57.3	269 <sup>+56.3</sup> <sub>-28.9</sub>	125 <sup>+77.8</sup> <sub>-116</sub>	0.28 <sup>+0.06</sup> <sub>-0.08</sub>	0.31 ± 0.06	0.00 <sup>+0.15</sup> <sub>-0.000</sub>
Best-fit	(230)	(259)	(45.9)	(0.26)	(0.31)	(0.00)
ΔBackground	+25.8 (±63)	-11.4 (±55.3)	-52.4 ( <sup>+173</sup> <sub>-73</sub> )	-0.025 (±0.06)	-0.077 (±0.06)	±0 ( <sup>+0.18</sup> <sub>-0.00</sub> )
ΔSpectral	-34.6 ( <sup>+90.6</sup> <sub>-24.9</sub> )	+18.6 ( <sup>+40.2</sup> <sub>-21.2</sub> )	-125 ( <sup>+180</sup> <sub>-0</sub> )	+0.03 ( <sup>+0.05</sup> <sub>-0.09</sub> )	+0.02 (±0.07)	+0.003 ( <sup>+0.13</sup> <sub>-0.00</sub> )
ΔDistance	+20.2 ( <sup>+53.8</sup> <sub>-107</sub> )	-97.9 (±54.7)	-125 ( <sup>+294</sup> <sub>-23.7</sub> )	+0.03 ( <sup>+0.05</sup> <sub>-0.08</sub> )	+0.00 (±0.07)	+0.10 ( <sup>+0.29</sup> <sub>-0.10</sub> )
ΔKnots	+58.2 ( <sup>+37.9</sup> <sub>-53.5</sub> )	+11.7 ( <sup>+41</sup> <sub>-20.2</sub> )	±120 ( <sup>+114</sup> <sub>-53.5</sub> )	+0.02 ( <sup>+0.05</sup> <sub>-0.09</sub> )	-0.043 (±0.07)	+0.28 (±0.07)
ΔFit priors	+33.3 ( <sup>+33.3</sup> <sub>-24.5</sub> )	+126 ( <sup>+47.5</sup> <sub>-112</sub> )	+188 (±169)	+0.03 ( <sup>+0.08</sup> <sub>-0.11</sub> )	+0.05 (±0.10)	+0.06 ( <sup>+0.15</sup> <sub>-0.06</sub> )
ΔEntropy	+1.69 (±60.6)	-10.8 ( <sup>+58.2</sup> <sub>-26.4</sub> )	-67 ( <sup>+125</sup> <sub>-58.3</sub> )	+0.01 ( <sup>+0.04</sup> <sub>-0.10</sub> )	+0.03 (±0.09)	+0.006 ( <sup>+0.16</sup> <sub>-0.01</sub> )
ΔCovariance	+29 ( <sup>+99.9</sup> <sub>-35.1</sub> )	±19.2 ( <sup>+77.1</sup> <sub>-54.5</sub> )	-122 ( <sup>+125</sup> <sub>-70.8</sub> )	+0.03 ( <sup>+0.09</sup> <sub>-0.12</sub> )	+0.05 ( <sup>+0.10</sup> <sub>-0.07</sub> )	+0.001 ( <sup>+0.05</sup> <sub>-0.00</sub> )
ΔWeighting	-9.86 (±49.4)	+47.8 ( <sup>+36.8</sup> <sub>-53.9</sub> )	-63.7 ( <sup>+377</sup> <sub>-61.7</sub> )	-0.013 ( <sup>+0.06</sup> <sub>-0.07</sub> )	+0.02 ( <sup>+0.06</sup> <sub>-0.07</sub> )	±0 ( <sup>+0.14</sup> <sub>-0.00</sub> )

**Table 1.** Marginalized values and 1- $\sigma$  confidence regions for  $v_{eff}$  and  $f_{nth}$  measured at three representative radii. Since the best-fitting parameters need not be identical to the marginalized values, we also list the best-fitting values for each parameter (in parentheses). In addition to the statistical errors, we also show estimates of the error budget from possible sources of systematic uncertainty. We consider a range of different systematic effects, which are described in detail in § 4.2; specifically we evaluate the effect of treatment of the background ( $\Delta$ Background), spectral-fitting choices ( $\Delta$ Spectral), distance uncertainties ( $\Delta$ Distance), the number of spline knots used in the calculation ( $\Delta$ Knots), priors on the fit parameters ( $\Delta$ Fit priors), the entropy parameterization ( $\Delta$ Entropy), treatment of the covariance between data-points ( $\Delta$ Covariance) and disabling the emissivity computation ( $\Delta$ Weighting). We list the change in the marginalized value of each parameter for every test and, in parentheses, the statistical uncertainty on the parameter determined from the test. Note that the systematic error estimates should *not* in general be added in quadrature with the statistical error

tailored to match real observations of the representative, bright system NGC 4649. At unresolved scales, the recovered distributions of  $v_{eff}$  and  $f_{nth}$  were approximately correct, but were sensitive to the exact parameterizations used to fit them.

The approach outlined here did not allow us to break the degeneracy between bulk gas motions ( $v_{eff}$ ) and non-thermal pressure ( $f_{nth}$ ), and so we advocated determining each profile separately. In a real system, it is likely that some combination of both effects could contribute to non-thermal support, and so it is desirable to fold in additional constraints to try to disentangle them. This can be easily implemented in a Bayesian framework by modifying the priors appropriately. In principle, resonance scattering measurements, or spectral line broadening constraints, could be employed in this way as restrictions on the turbulent pressure component of  $f_{nth}$ . Similarly, magnetic field rotation measure constraints could be employed to restrict the magnetic pressure contribution to  $f_{nth}$ . As discussed in B09, the ellipticity profile of the gas actually provides important information on the gas motion, potentially allowing it to be used as an indirect constraint on  $v_{eff}$ . To do this fully self-consistently, as in B09, involves running a suite of hydrodynamical models, making it impractical to cover a suitably large region of parameter space. With significant simplifications, for example assuming that the only gas motions are rotational, the problem becomes tractable. Unfortunately, to evaluate the models properly then involves relaxing the spherical approximation, which substantially complicates the analysis beyond the scope of this paper. Non-spherical hydrostatic models including rotation have been constructed before (e.g. Buote & Canizares 1996; Statler & McNamara 2002), but not for computing detailed temperature and density distributions.

As presented here, the model provides a means for measuring deviations from hydrostatic equilibrium in the gas.

Conversely, if a physical model exists for  $v_{eff}$  or  $f_{nth}$ , the same approach could be used to correct the X-ray mass measurement for deviations from hydrostatic equilibrium, making X-ray studies alone of nearby galaxies potentially suitable for high-precision cosmology. At the moment, our understanding of nonthermal support in the centres of galaxies is still in its infancy, but when the  $v_{eff}$  and  $f_{nth}$  profiles of sufficiently large a sample of systems have been measured, this may become routine.

## 5.2 Nonthermal support in NGC 4649

Applying our model to NGC 4649, we have carried out a joint stellar dynamical and X-ray mass analysis, effectively reconciling the measurements made by Shen & Gebhardt (2010) and Humphrey et al. (2008) with a modest but significant ( $\sim 25\%$ ) nonthermal pressure profile. We obtained these estimates by assuming that the ISM is maintained in static equilibrium, whereas in practice, we expect there to be a modest cooling flow (e.g. B09). The measured level of nonthermal support will then be an overestimate, albeit only very slightly if the cooling flow is very subsonic. By comparing the mass profiles obtained from stellar dynamical and X-ray analysis (Fig 1), Das et al. (2010) similarly concluded that the nonthermal pressure in NGC 4649 is no larger than  $\sim 32\%$ , although they did not present a detailed  $f_{nth}$  profile. *This level of deviation from hydrostatic equilibrium is fully comparable to that expected in galaxy clusters, which are routinely used for cosmology* (e.g. Tsai et al. 1994; Buote & Tsai 1995; Evrard et al. 1996; Rasia et al. 2006; Nagai et al. 2007; Piffaretti & Valdarnini 2008; Fang et al. 2009; Lau et al. 2011), and is consistent with (albeit slightly larger than inferred in) the conclusions of Churazov et al. (2008) for two more morphologically disturbed systems. Considering the level of statistical and systematic errors in our previous studies of early-type galaxies (e.g. Humphrey et al.

2006, 2008, 2009, 2011, 2012a,b), this level of nonthermal pressure, if ubiquitous, would not imply qualitatively different conclusions on the gravitating mass profiles.

Since the level of nonthermal support is inferred from the subtle differences between the mass profiles derived with two techniques, control of the systematic errors is important for a robust measurement. Certain choices, such as the treatment of the X-ray background, the adopted fit priors, and the number of spline knots used, can have a non-negligible impact on the recovered profile, as is clear from § 4.2. Given present uncertainties (both statistical and systematic), the data currently do not allow us to determine whether the nonthermal support profiles ( $v_{eff}$  or  $f_{nth}$ ) are constant with radius (as assumed by Churazov et al. 2008), or if they are gradually declining; they are clearly consistent with zero outside  $\sim 5$  kpc. While we anticipate improved statistical X-ray constraints if we fold in the available archival *XMM* data and the significantly deeper *Chandra* observations ( $\sim 200$  ks, as compared to the 81 ks used in our analysis) that will soon be publicly available in the archive, the large statistical uncertainty on the current optically inferred mass at large radii (Fig 1) is a major limiting factor.

At present, we have not folded in any systematic errors in the stellar dynamical analysis into our study. In particular, uncertainties in the inclination of the system may be important (e.g. Thomas et al. 2007). Shen & Gebhardt (2010) explored different inclination angles with a simplified model that included a fixed dark matter halo, finding that inclination had little impact on their results. Given the restricted parameter space explored in this way, we did not attempt to incorporate these fits onto our work and marginalize over inclination. More intriguing are the recent particle based models of Das et al. (2011), who found much larger confidence regions for the enclosed mass profiles than Shen & Gebhardt when fitting kinematic data for the stars and planetary nebulae, implying a lower level of nonthermal support than measured here. Some of the discrepancies with the Shen & Gebhardt results may arise in part due to there being different equilibrium configurations for the globular cluster and the planetary nebulae populations. However, this should not be important in the central part of the galaxy, where the inferred nonthermal pressure is strongest. This is supported by the good agreement between the stellar M/L ratios inferred by Shen & Gebhardt and Gebhardt et al. (2003), who used only stellar kinematics. While we expect the state of the art dynamical modelling of Shen & Gebhardt to be robust, it is unclear why the code used by Das et al. produced such a different result. Until this tension is resolved, some questions persist over the exact level of nonthermal support in NGC 4649. As it stands, the true level of nonthermal support may be lower than we infer. Nevertheless, in the following sections, we consider the physical implications of nonthermal support at the level inferred in our study.

### 5.2.1 Gas rotation

Given the smooth, relaxed isophotes of NGC 4649, we would not expect large-scale bulk gas motions other than, perhaps, gas rotation, which is expected in the centre of a cooling flow (e.g. Nulsen et al. 1984; Kley & Mathews 1995; Brighenti & Mathews 1996). B09 computed detailed hydrodynamical models for the gas flow in NGC 4649, which they tailored to

match the gas density, temperature and ellipticity profiles. They concluded that rotation could be dynamically important within the central  $\sim$ kpc. Comparison of their inferred  $v_{eff}$  profile (Fig 3, left panel) to the real data (Fig 5, left panel) strongly suggests that, while rotation could dominate the nonthermal support at these small scales, it cannot explain the observations at larger scales ( $\sim 1-3$  kpc). It is likely that B09 underestimated the level of gas rotation, as they adopted the gravitational potential inferred from the hydrostatic fit, rather than the deeper (true?) potential from dynamics, but the modest underestimate in  $v_{eff}$  that is implied in order to maintain the same level of isophotal flattening ( $\lesssim 20\%$ ) will still not reconcile the simulated rotation velocity with the observed profile at these scales.

### 5.2.2 Random turbulence

Alternatively, the nonthermal pressure profile ( $f_{nth}$ ) could arise due to turbulent motions within the gas. Assuming isotropic turbulence and eddy velocities drawn from a Maxwell-Boltzmann distribution, the turbulent pressure is given by  $P_t \simeq (1/3)\rho_g v_{turb}^2$ , where  $v_{turb}$  is the r.m.s. turbulent velocity. Adopting  $kT=0.8$  keV, we find that  $v_{turb} \simeq 600\sqrt{f_{nth}/(1-f_{nth})}$  km s $^{-1}$ , or  $\sim 360 \pm 60$  km s $^{-1}$  for  $f_{nth}=0.27 \pm 0.06$ . Random turbulence of this magnitude may help to generate a dynamically important magnetic field that would also contribute nonthermal pressure (see § 5.2.4). Whether plausible sources of random turbulence, such as mixing from stellar mass loss and Type Ia supernovae, galaxy merging and “sloshing”, or AGN-driven disturbances in the ISM are sufficient to maintain turbulence at this level is unclear.

Turbulent diffusion can provide a means for transporting angular momentum outwards, counteracting the ISM rotation that is expected to be induced by inflow, and thus making the X-ray image rounder (Brighenti & Mathews 2000). Although sensitive to the assumed length-scale of the largest turbulent eddies, B09 used the isophotal flattening in the core of NGC 4649 to infer turbulent velocities  $\sim 50$  km s $^{-1}$ , which are not dynamically important.

It is worthwhile to compare the inferred level of turbulence with that implied in the centres of elliptical galaxies from other means. Sanders et al. (2011) placed an upper limit of  $700$  km s $^{-1}$  on line broadening in the *XMM* RGS spectrum of NGC 4649, which is too large to be interesting. While Werner et al. (2009) were not able to place useful constraints on resonance scattering in NGC 4649, they measured the effect in three other similar galaxies, including NGC 4636, for which they inferred  $v_{turb} < 100$  km s $^{-1}$ . Conversely de Plaa et al. (2012) inferred significant turbulence ( $\sim 140-700$  km s $^{-1}$ ) in two other systems, which may be consistent with our observation of NGC 4649. However, we note that, for one of these systems, NGC 5044, Sanders et al. (2011) concluded that the width of the spectral lines in RGS spectra was fully consistent with the source just being spatially extended, leaving little room for turbulent broadening. Whether turbulence as large as  $\sim 360$  km s $^{-1}$  is realistic in the centre of a giant elliptical galaxy therefore remains unclear at this point, but it does not appear ubiquitous. Still, this may be resolved by observations with *Astro-H* (§ 5.3).

### 5.2.3 Cosmic Ray Pressure

Another possible cause of nonzero  $f_{nth}$  is cosmic ray pressure. Strong cosmic ray injection into the ISM from the radio jet is likely to inflate large cavities (e.g. Mathews & Brighenti 2008), which are not seen in NGC 4649 (Humphrey et al. 2008). Still, it remains plausible that there could be non-negligible cosmic ray pressure in the vicinity of the (weak) jets, which extend for  $\lesssim 1.5$  kpc (Shurkin et al. 2008). Intriguingly, our current measurement (Fig 5) is consistent with  $f_{nth}$  being significantly weaker outside the central  $\sim 2$  kpc. In fact, the fit is formally indistinguishable if the nonthermal pressure is set to zero at these scales ( $\chi^2/\text{dof}=19.6/16$ , as compared to 18.7/13). If cosmic ray injection is primarily responsible for the nonthermal support in NGC 4649 and similar objects, we would expect to see a strong correlation between the radii requiring  $f_{nth} \neq 0$  and the extent of the jets. This is potentially testable as the jet morphology differs widely in nearby galaxies that are accessible for this kind of joint X-ray-optical analysis.

### 5.2.4 Magnetic Fields

Observationally, there are known to be  $\gtrsim \mu\text{G}$  magnetic fields in the centres of some early-type galaxies (Vallée 2011), which may provide an additional source of nonthermal pressure. For an early-type galaxy, a plausible mechanism for maintaining such a field would be the turbulent dynamo effect (e.g. Mathews & Brighenti 1997; Brandenburg & Subramanian 2005). Assuming that the entire nonthermal pressure is provided by this mechanism, and assuming equipartition between the magnetic and turbulent energy densities (which should maintain a disordered field), we computed the B-field required in NGC 4649, using  $P_{mag} = B^2/8\pi$ , where  $P_{mag}$  is the magnetic pressure and  $B$  is the B-field in cgs units. The implied field strength profile, shown in Fig 6 (left panel), falls steeply with radius (roughly  $B = 24(R/\text{kpc})^{-0.8} \mu\text{G}$ ) and requires turbulent velocities,  $v_{turb} \simeq 230 \text{ km s}^{-1}$ . The radial B-field dependence is similar to what is expected from simple galaxy formation models (Mathews & Brighenti 1997; Beck et al. 2012), and comparable fields have been inferred at small scales in a few galaxies with embedded radio jets (Vallée 2011), albeit such strong fields are not ubiquitous.

In the right hand panel of Fig 6, we show how the implied B-field varies with the electron density. The data were well fitted ( $\chi^2/\text{dof}=1.1/4$ ) with a model  $B = B_0 (n_e/0.1 \text{ cm}^{-3})^\gamma$ , where  $B_0 = 39 \pm 6 \mu\text{G}$  and  $\gamma = 0.59 \pm 0.09$ . We note that this is similar to the predictions of magnetic field generation in a (nonrotating) cooling flow predicted by Mathews & Brighenti (1997), albeit the field strength is much higher (Fig 6). Faraday rotation measure constraints in some galaxy clusters imply  $\gamma$  ranging from  $\sim 0.5$ – $1.0$  (e.g. Dolag et al. 2001; Guidetti et al. 2008), similar to our inferred value for NGC 4649.

## 5.3 Measuring gas motions with *Astro-H*

If turbulence or bulk gas motions are primarily responsible for the nonthermal support in NGC 4649, we should see associated Doppler broadening or centroid shifts of the X-ray emission lines. Given the spatially extended nature of

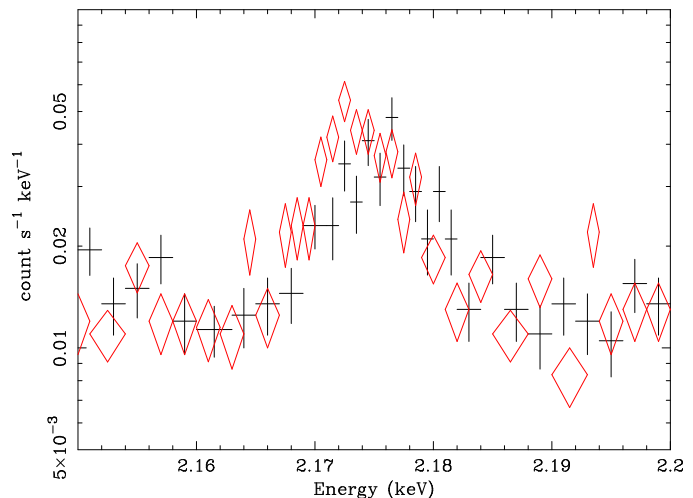


**Figure 7.** Portions of two simulated *Astro-H* SXS spectra, showing a Si XIII line. The spectra were accumulated from the entire SXS field of view in two different pointings, which were centred at different positions along the major axis of NGC 4649, symmetrically about the core of the galaxy. The simulations assumed that nonthermal support was entirely due to gas rotation; the Doppler shifting of the X-ray lines produces a clear shift in the line centroid between the two spectra (shown as crosses and diamonds). For illustration purposes, the simulated spectra shown have 1 Ms exposures, as opposed to the 200 ks exposures discussed in the text.

the hot gas, no currently in-orbit instrument would allow these modest shifts to be measured definitively. However, the nondispersive, high resolution spectroscopy enabled by microcalorimeters scheduled to fly on future missions is ideally suited to this task.

Of particular interest is the Soft X-ray Spectrometer (SXS) aboard the *Astro-H* observatory (Takahashi et al. 2010). To explore whether it will be possible to measure the predicted gas motions in NGC 4649 with this instrument, we simulated two deep ( $\sim 200$  ks) exposures, each centred along the major axis at a distance  $\sim 1.5'$  from the galaxy core. Spectra were extracted from the entire  $3 \times 3'$  field of view in each case. If the gas is rotating, one spectrum should be redshifted, and one blueshifted. To simulate the spectra, we modified the Monte Carlo approach outlined in § 3.3. At a series of grid positions  $(R, \theta, z)$ , we generated photons, assuming a thermally broadened APEC plasma with a given density, temperature, abundance, line-of-sight velocity and (turbulent) Doppler line broadening. These parameters were derived from the best-fitting models, assuming spherical symmetry. Assuming isotropy, turbulence should produce Gaussian broadening of the line,  $I \propto \exp(-(E - E_0)^2/\Delta E^2)$ , where  $E_0$  is the line centre, and  $\Delta E/E = \sqrt{2/3} v_{turb}/c \equiv b/c$ , where  $b$  is the Doppler b-parameter.

To incorporate the sensitivity of the SXS, we used the standard “baseline” on-axis *Astro-H* responses, `ah_sxs_7ev_basefilt_20090216.rmf` and `sxt-s_100208_ts02um_of_intallpx1.arf`<sup>5</sup>. Photons were then projected onto the sky, folding in the nominal on-axis

<sup>5</sup> <http://astro-h.isas.jaxa.jp/researchers/sim/response.html>

point spread function (the ‘‘ah\_sxt\_psfmodel\_20090217’’ model)<sup>6</sup>. Additional background photons were generated, corresponding to emission from low mass X-ray binaries (a 7.3 keV bremsstrahlung model distributed like the stellar light and normalized according to the measurement of Humphrey & Buote 2008), the cosmic X-ray background (a powerlaw with  $\Gamma=1.41$  and normalization given by De Luca & Molendi 2004), the Galactic foreground (a 0.07 keV and a 0.20 keV APEC plasma component, e.g. Humphrey et al. 2011) and emission from the Virgo cluster ICM (a 2.5 keV APEC component; Humphrey et al. 2008). For simplicity, we ignored the (featureless) instrumental background which is at least an order of magnitude fainter than the source emission below  $\sim 3$  keV.

Since there was a range of gas temperatures projected into the field of view, we modelled the background-subtracted spectrum using two APEC models with (the same) Doppler broadening and tied abundances and redshifts, plus a bremsstrahlung model to account for LMXBs. We found this model adequately fitted the spectra. If gas rotation supplies the nonthermal support, we would expect a peak  $\sim 500\text{km s}^{-1}$  velocity gradient between the two fields, which corresponds to  $\sim 4$  eV at 2.2 keV. In practice, the large apertures used caused the line profiles to be smeared out. Nevertheless, as shown in Fig 7, the line centroid shift should be detectable; for 200 ks exposures, we expect to detect the gas rotation at  $\sim 4\sigma$ . Conversely, if turbulence dominates the gas dynamics, we would expect  $\sim 200\text{km s}^{-1}$  broadening of the lines, and little velocity gradient. Simulating corresponding spectra, we found the line broadening was required; we constrained the line of sight rms velocity to  $180 \pm 40\text{km s}^{-1}$ . *Therefore, if gas motions are responsible for the nonthermal support in NGC 4649, we expect to be able to measure them with Astro-H.*

## ACKNOWLEDGMENTS

We would like to thank Taotao Fang and Fabio Gastaldello for discussions. PJH and DAB gratefully acknowledge partial support from NASA under Grant NNX10AD07G, issued through the office of Space Science Astrophysics Data Program.

## APPENDIX A: COMPARISON WITH X-RAY ANALYSIS OF DAS ET AL.

Das et al. (2010) introduced a minimally parametric method for recovering the mass profiles of systems in which the gas is approximately hydrostatic, by inverting the temperature and density profile data. Their approach is a variant of the ‘‘smoothed inversion’’ technique (for a critical review of mass modelling techniques, see Buote & Humphrey 2012a), in which, rather than fitting smooth models to the density and temperature profile, they instead apply a smoothing prior, controlled by the parameter  $\lambda$ , which is calibrated against realistic data. They assumed that  $\lambda$  is the same (and fixed) for all observables (temperature, density, rotation velocity) and all systems. The advantage of this method is that it

makes few *a priori* assumptions about the shape of the mass or temperature profiles. The disadvantage is that it assumes that all of the profiles are smooth in a particular manner, which is the same for all profiles<sup>7</sup>.

In Fig 1, we compare the  $v_c$  profiles obtained by our method and by Das et al. (2010). In general, the agreement is good over the range  $\sim 3\text{--}9$  kpc, but the mass found by Das et al. (2010) is higher outside of this range. In Fig A1, we compare the temperature and density data which were fitted in our analysis, and those used by Das et al.. It is immediately clear that there is good agreement between all three data-sets between  $\sim 3\text{--}9$  kpc, where the  $v_c$  profiles also agree, but discrepancies arise outside this range. We conclude that the differences between the mass inferred from the hydrostatic analysis of Das et al. (2010) and Humphrey et al. (2008) are most probably a consequence of the different *temperature and density profiles*, rather than intrinsic differences in the mass fitting techniques.

At the smallest scales, there is a large difference between the *XMM* and *Chandra* data-points, which probably reflects the larger PSF of *XMM* (90% encircled energy radius  $\simeq 30'' = 2.2$  kpc) compromising the inner data by spectral mixing between adjacent annuli. This offset may explain the formally poor reduced  $\chi^2$  ( $\simeq 6$ ) obtained by Das et al. in their fits. We note that such large systematic errors will distort the  $\chi^2$  topology, even if the best-fitting model is correct, compromising the error-bar calculation.

The remaining differences with our *Chandra* profiles (in particular the lower temperature we found at large scales) probably reflect different analysis choices made by Churazov et al. (2010a), who derived the profiles used by Das et al.. Specifically, in their analysis the ISM abundance was fixed to a constant value ( $Z_{\text{Fe}}=0.5$ ), and Solar abundance ratios were used for all species, which is not formally correct for NGC 4649 (Humphrey & Buote 2006; Humphrey et al. 2006; B09). Furthermore, they ignored the contribution of unresolved LMXBs (which can affect the inferred density) and projected emission from the Virgo ICM (which can affect the temperature) in their fits, while their correction for projected emission from gas beyond the outermost shells used in the deprojection did not account for the truncation of the halo by the Virgo ICM. In our modelling, we explicitly accounted for these effects (Humphrey et al. 2008). Nevertheless, even with the different analysis choices, we see that the recovered mass profile is not dramatically affected over most of the interesting radial range (Fig 1).

## REFERENCES

- Abadi M. G., Navarro J. F., Fardal M., Babul A., Steinmetz M., 2010, MNRAS, 407, 435
- Barnabè M., Czoske O., Koopmans L. V. E., Treu T., Bolton A. S., 2011, MNRAS, 415, 2215
- Beck A. M., Lesch H., Dolag K., Kotarba H., Geng A., Staszyn F. A., 2012, MNRAS, in press (arXiv:1202.3349)
- Biller B. A., Jones C., Forman W. R., Kraft R., Ensslin T., 2004, ApJ, 613, 238

<sup>7</sup> Compare this with the forward fitting method, which imposes (generally smooth) functional forms on the gravitating mass and entropy profile.

<sup>6</sup> [http://astro-h.isas.jaxa.jp/researchers/sim/GSFC\\_mirror.html](http://astro-h.isas.jaxa.jp/researchers/sim/GSFC_mirror.html)

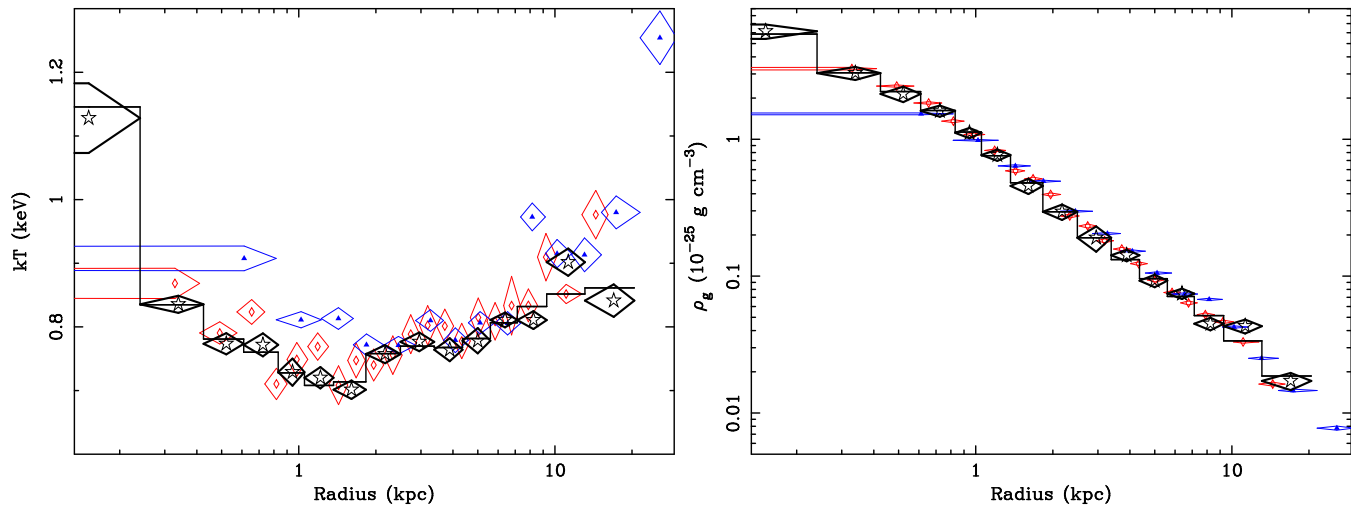


**Figure A1.** *Left panel:* *Chandra* temperature profile obtained by Humphrey et al. (2008) (black stars), compared to the profiles used by Das et al. (2010) (*Chandra*: red diamonds, *XMM*: blue triangles). Note the general agreement between the *Chandra* profiles inside  $\sim 10$  kpc, but the disagreement with *XMM* at the smallest scales. *Right panel:* The same for the gas density profiles. Since the density profiles were shown with arbitrary normalization in Das et al. (2010), we have arbitrarily scaled them here for clarity.

Binney J., Tremaine S., 2008, *Galactic Dynamics*, 2<sup>nd</sup> ed.; Princeton, NJ: Princeton University Press  
 Blumenthal G. R., Faber S. M., Flores R., Primack J. R., 1986, *ApJ*, 301, 27  
 Böhringer H., Briel U. G., Schwarz R. A., Voges W., Hartner G., Trümper J., 1994, *Nature*, 368, 828  
 Bolton A. S., Burles S., Treu T., Koopmans L. V. E., Moustakas L. A., 2007, *ApJ*, 665, L105  
 Brandenburg A., Subramanian K., 2005, *Phys. Rep.*, 417, 1  
 Brighenti F., Mathews W. G., 1996, *ApJ*, 470, 747  
 Brighenti F., Mathews W. G., 2000, *ApJ*, 539, 675  
 Brighenti F., Mathews W. G., Humphrey P. J., Buote D. A., 2009, *ApJ*, 705, 1672, (B09)  
 Bullock J. S., Kolatt T. S., Sigad Y., Somerville R. S., Kravtsov A. V., Klypin A. A., Primack J. R., Dekel A., 2001, *MNRAS*, 321, 559  
 Buote D. A., Canizares C. R., 1994, *ApJ*, 427, 86  
 Buote D. A., Canizares C. R., 1996, *ApJ*, 457, 177  
 Buote D. A., Canizares C. R., 1998, *MNRAS*, 298, 811  
 Buote D. A., Humphrey P. J., 2012a, in D.-W. Kim & S. Pellegrini, ed., *Astrophysics and Space Science Library*, 235, (arXiv:1104.0012)  
 Buote D. A., Humphrey P. J., 2012b, *MNRAS*, 420, 1693  
 Buote D. A., Humphrey P. J., 2012c, *MNRAS*, 421, 1399  
 Buote D. A., Jeltema T. E., Canizares C. R., Garmire G. P., 2002, *ApJ*, 577, 183  
 Buote D. A., Tsai J. C., 1995, *ApJ*, 439, 29  
 Cappellari M. et al., 2006, *MNRAS*, 366, 1126  
 Cappellari M. et al., 2012, *Nature*, in press (arXiv:1202.3308)  
 Cavagnolo K. W., Donahue M., Voit G. M., Sun M., 2009, *ApJS*, 182, 12  
 Churazov E., Forman W., Vikhlinin A., Tremaine S., Gerhard O., Jones C., 2008, *MNRAS*, 388, 1062  
 Churazov E. et al., 2010a, *MNRAS*, 359  
 Churazov E., Zhuravleva I., Sazonov S., Sunyaev R., 2010b, *Space Sci. Rev.*, 157, 193

Ciotti L., Pellegrini S., 2004, *MNRAS*, 350, 609  
 Das P., Gerhard O., Churazov E., Zhuravleva I., 2010, *MNRAS*, 409, 1362  
 Das P., Gerhard O., Mendez R. H., Teodorescu A. M., de Lorenzi F., 2011, *MNRAS*, 415, 1244  
 De Luca A., Molendi S., 2004, *A&A*, 419, 837  
 de Plaa J., Zhuravleva I., Werner N., Kaastra J. S., Churazov E., Smith R. K., Raassen A. J. J., Grange Y. G., 2012, *A&A*, 539, A34  
 Dolag K., Schindler S., Govoni F., Feretti L., 2001, *A&A*, 378, 777  
 Dutton A. A., van den Bosch F. C., Dekel A., Courteau S., 2007, *ApJ*, 654, 27  
 El-Zant A. A., Hoffman Y., Primack J., Combes F. and Shlosman I., 2004, *ApJ*, 607, L75  
 Evrard A. E., Metzler C. A., Navarro J. F., 1996, *ApJ*, 469, 494  
 Fang T., Humphrey P., Buote D., 2009, *ApJ*, 691, 1648  
 Feroz F., Hobson M. P., Bridges M., 2009, *MNRAS*, 398, 1601  
 Ferrarese L., Ford H., 2005, *Space Sci. Rev.*, 116, 523  
 Forman W. et al., 2007, *ApJ*, 665, 1057  
 Fukazawa Y., Botoya-Nonesca J. G., Pu J., Ohto A., Kawano N., 2006, *ApJ*, 636, 698  
 Gastaldello F., Buote D. A., Humphrey P. J., Zappacosta L., Brighenti F., Mathews W. G., 2007a, in Böhringer H., Pratt G. W., Finoguenov A., Schuecker P., eds., *Heating versus Cooling in Galaxies and Clusters of Galaxies*, 275  
 Gastaldello F., Buote D. A., Humphrey P. J., Zappacosta L., Bullock J. S., Brighenti F., Mathews W. G., 2007b, *ApJ*, 669, 158  
 Gavazzi R., 2005, *A&A*, 443, 793  
 Gavazzi R., Treu T., Rhodes J. D., Koopmans L. V. E., Bolton A. S., Burles S., Massey R. J., Moustakas L. A., 2007, *ApJ*, 667, 176  
 Gebhardt K., Thomas J., 2009, *ApJ*, 700, 1690  
 Gebhardt K. et al., 2000, *AJ*, 119, 1157  
 Gebhardt K. et al., 2003, *ApJ*, 583, 92

- Gerhard O., Kronawitter A., Saglia R. P., Bender R., 2001, *AJ*, 121, 1936
- Gnedin O. Y., Kravtsov A. V., Klypin A. A., Nagai D., 2004, *ApJ*, 616, 16
- Gnedin O. Y., Weinberg D. H., Pizagno J., Prada F., Rix H.-W., 2007, *ApJ*, 671, 1115
- Guidetti D., Murgia M., Govoni F., Parma P., Gregorini L., de Ruiter H. R., Cameron R. A., Fanti R., 2008, *A&A*, 483, 699
- Gültekin K. et al., 2009, *ApJ*, 698, 198
- Humphrey P. J., Buote D. A., 2006, *ApJ*, 639, 136
- Humphrey P. J., Buote D. A., 2008, *ApJ*, 689, 983
- Humphrey P. J., Buote D. A., 2010, *MNRAS*, 403, 2143
- Humphrey P. J., Buote D. A., Brighenti F., Flohic H. M. L. G., Gastaldello F., Mathews W. G., 2012a, *ApJ*, 748, 11
- Humphrey P. J., Buote D. A., Brighenti F., Gebhardt K., Mathews W. G., 2008, *ApJ*, 683, 161
- Humphrey P. J., Buote D. A., Brighenti F., Gebhardt K., Mathews W. G., 2009, *ApJ*, 703, 1257
- Humphrey P. J., Buote D. A., Canizares C. R., Fabian A. C., Miller J. M., 2011, *ApJ*, 729, 53
- Humphrey P. J., Buote D. A., Gastaldello F., Zappacosta L., Bullock J. S., Brighenti F., Mathews W. G., 2006, *ApJ*, 646, 899
- Humphrey P. J., Buote D. A., O'Sullivan E., Ponman T. J., 2012b, *ApJ*, submitted (arXiv:1204.3095)
- Irwin J. A., Sarazin C. L., 1996, *ApJ*, 471, 683
- Johnson R., Chakrabarty D., O'Sullivan E., Raychaudhury S., 2009, *ApJ*, 706, 980
- Kley W., Mathews W. G., 1995, *ApJ*, 438, 100
- Koopmans L. V. E. et al., 2009, *ApJ*, 703, L51
- Kormendy J., Fisher D. B., Cornell M. E., Bender R., 2009, *ApJS*, 182, 216
- Kormendy J., Richstone D., 1995, *ARA&A*, 33, 581
- Lau E. T., Nagai D., Kravtsov A. V., Zentner A. R., 2011, *ApJ*, 734, 93
- Long R. J., Mao S., 2012, arXiv:1201.0951
- Macciò A. V., Dutton A. A., van den Bosch F. C., 2008, *MNRAS*, 391, 1940
- Macciò A. V., Stinson G., Brook C. B., Wadsley J., Couchman H. M. P., Shen S., Gibson B. K., Quinn T., 2012, *ApJ*, 744, L9
- Mathews W. G., Brighenti F., 1997, *ApJ*, 488, 595
- Mathews W. G., Brighenti F., 2003a, *ARA&A*, 41, 191
- Mathews W. G., Brighenti F., 2003b, *ApJ*, 599, 992
- Mathews W. G., Brighenti F., 2008, *ApJ*, 676, 880
- Merritt D., Ferrarese L., 2001, *ApJ*, 547, 140
- Million E. T., Werner N., Simionescu A., Allen S. W., Nulsen P. E. J., Fabian A. C., Böhringer H., Sanders J. S., 2010, *MNRAS*, 407, 2046
- Murphy J. D., Gebhardt K., Adams J. J., 2011, *ApJ*, 729, 129
- Nagai D., Vikhlinin A., Kravtsov A. V., 2007, *ApJ*, 655, 98
- Napolitano N. R., Romanowsky A. J., Tortora C., 2010, *MNRAS*, 405, 2351
- Navarro J. F., Frenk C. S., White S. D. M., 1997, *ApJ*, 490, 493
- Norris M. A. et al., 2012, ArXiv e-prints
- Nulsen P. E. J., Stewart G. C., Fabian A. C., 1984, *MNRAS*, 208, 185
- Ota N. et al., 2007, *PASJ*, 59, 351
- Pellegrini S., Ciotti L., 2006, *MNRAS*, 370, 1797
- Piffaretti R., Valdarnini R., 2008, *A&A*, 491, 71
- Randall S. W., Sarazin C. L., Irwin J. A., 2004, *ApJ*, 600, 729
- Rasia E. et al., 2006, *MNRAS*, 369, 2013
- Romanowsky A. J., Douglas N. G., Arnaboldi M., Kuijken K., Merrifield M. R., Napolitano N. R., Capaccioli M., Freeman K. C., 2003, *Science*, 301, 1696
- Romanowsky A. J., Strader J., Spitler L. R., Johnson R., Brodie J. P., Forbes D. A., Ponman T., 2009, *AJ*, 137, 4956
- Rusli S. P., Thomas J., Erwin P., Saglia R. P., Nowak N., Bender R., 2011, *MNRAS*, 410, 1223
- Sanders J. S., Fabian A. C., Smith R. K., 2011, *MNRAS*, 410, 1797
- Sato K., Matsushita K., Ishisaki Y., Yamasaki N. Y., Ishida M., Sasaki S., Ohashi T., 2008, *PASJ*, 60, 333
- Shen J., Gebhardt K., 2010, *ApJ*, 711, 484
- Shurkin K., Dunn R. J. H., Gentile G., Taylor G. B., Allen S. W., 2008, *MNRAS*, 383, 923
- Statler T. S., McNamara B. R., 2002, *ApJ*, 581, 1032
- Sugawara C., Takizawa M., Nakazawa K., 2009, *PASJ*, 61, 1293
- Sun M., Voit G. M., Donahue M., Jones C., Forman W., Vikhlinin A., 2009, *ApJ*, 693, 1142
- Takahashi T. et al., 2010, in , Society of Photo-Optical Instrumentation Engineers (SPIE) Conference Series
- Tamura T., Hayashida K., Ueda S., Nagai M., 2011, *PASJ*, 63, 1009
- Thomas J., Jesseit R., Naab T., Saglia R. P., Burkert A., Bender R., 2007, *MNRAS*, 381, 1672
- Tonry J. L., Dressler A., Blakeslee J. P., Ajhar E. A., Fletcher A., Luppino G. A., Metzger M. R., Moore C. B., 2001, *ApJ*, 546, 681
- Treu T., Auger M. W., Koopmans L. V. E., Gavazzi R., Marshall P. J., Bolton A. S., 2010, *ApJ*, 709, 1195
- Trinchieri G., Fabbiano G., Kim D.-W., 1997, *A&A*, 318, 361
- Tsai J. C., Katz N., Bertschinger E., 1994, *ApJ*, 423, 553
- Vallée J. P., 2011, *New A. Rev.*, 55, 91
- Valluri M., Merritt D., Emsellem E., 2004, *ApJ*, 602, 66
- Werner N., Zhuravleva I., Churazov E., Simionescu A., Allen S. W., Forman W., Jones C., Kaastra J. S., 2009, *MNRAS*, 398, 23
- Wong K.-W., Irwin J. A., Yukita M., Million E. T., Mathews W. G., Bregman J. N., 2011, *ApJ*, 736, L23
- Xu H. et al., 2002, *ApJ*, 579, 600
- Zhuravleva I. V., Churazov E. M., Sazonov S. Y., Sunyaev R. A., Dolag K., 2011, *Astronomy Letters*, 37, 141